Selenium Valence-to-Core X-ray Emission Spectroscopy and Kβ HERFD X-ray Absorption Spectroscopy as Complementary Probes of Chemical and Electronic Structure

Justin T. Henthorn[1] and Serena DeBeer[1,*]

[1]Max Planck Institute for Chemical Energy Conversion, Stiftstrasse 34-36, D-45470 Mülheim an der Ruhr, Germany

Supporting Information Placeholder

ABSTRACT: Selenium X-ray absorption spectroscopy (XAS) has found widespread use in investigations of Se-containing materials, geochemical processes, and biological active sites. In contrast to sulfur Kβ X-ray emission spectroscopy (XES), which has been found to contain electronic and structural information complementary to S XAS, Se Kβ XES remains comparatively underexplored. Herein, we present the first Se Valence-to-Core (VtC) XES studies of reduced Se-containing compounds and FeSe dimers. Se VtC XES is found to be sensitive to changes in covalent Se bonding interactions (Se–Se/Se–C/Se–H bonding) while relatively insensitive to changes in Fe oxidation states as selenide bridges in FeSe dimers ($[Fe_2Se_2]^{2+}$ vs $[Fe_2Se_2]^+$). Contrastingly, Se Kβ HERFD XAS is demonstrated to be quite sensitive to changes in Fe-oxidation state, with Se Kβ HERFD XAS demonstrating experimental resolution equivalent to Kα HERFD XAS. Additionally, computational studies reveal both Se VtC XES and XAS to be sensitive to selenium protonation in FeSe complexes.

1 Introduction

Selenium is an essential trace element that plays pivotal functions in biological[1-3] and environmental sciences.[4] Additionally, selenium is a semiconductor with applications in the fields of nanoscience[5-6] and photovoltaics.[7-9] Other applications include energy storage[10-11] and glass manufacturing. Across many of these applications, there is great utility for an element selective spectroscopy to better understand the electronic and chemical structure of the relevant selenium species. ^{77}Se NMR has proven useful in characterizing the chemical environment of Se,[12-19] however the requirement of diamagnetic samples and

solution-based measurements limits its broad applicability as well as constrains its potential for *in situ* experiments. Se X-ray Absorption spectroscopy has been implemented in some of these applications.[20-25] Se XAS is directly analogous to S XAS, which has recently been coupled with S XES as a complementary probe of electronic and chemical structure.[26-27] By comparison, Se XES remains largely unexplored. Herein we report the first Se Kβ XES study of reduced Se compounds, including biologically relevant $[Fe_2Se_2]^{n+}$ complexes.

2 Experimental Methods

2.1 Sample preparation. Li_2Se and $[Et_4N][SeH]$ were synthesized following published procedures. KSeCN and gray (hexagonal) elemental Se (Se^o) were purchased from Sigma and used as received. The β-diketiminate supported iron dimer complexes $L_2Fe_2Se_2$ and $[K(THF)_6][L_2Fe_2Se_2]\cdot 2THF$ (L = $\{HC[C(CH_3)N-(2,6-^iPr_2C_6H_3)]_2\}^{1-}$) were prepared according to literature methods.[28] All synchrotron measurements were performed on solid samples diluted in BN (Sigma, dried under vacuum for 2 hours at 120°C) to approximately 1% Se by weight and finely ground with mortar and pestle, except KSeCN which was measured as a frozen 1mM solution in distilled H_2O. The solid samples were packed into 1mm thick aluminum spacers and sealed with 38 micron Kapton tape, while the KSeCN sample was prepared in a Delrin pinhole solution cell with a 38 micron Kapton tape window and frozen in liquid nitrogen.

2.2 Data collection and processing. All presented data were measured at beamline ID-26 of the European Synchrotron Radiation Facility (ESRF) with the storage ring operating at 6 GeV and injection currents of 90 mA in a 16-bunch filling mode. A Si(3 1 1) double-crystal monochromator was used upstream for

incident energy selection. The monochromatic incident energy was calibrated to the maximum of gray elemental selenium (12655.8 eV). The beam-size was 500x100 (horizontal x verticle) microns^2 providing a flux density of ~1×10^{12}ph/s. Selenium X-ray absorption spectra were measured simultaneously in total fluorescence yield (TFY) and $K\beta_1$ HERFD-detection modes. For the emission measurements, a 1 m radius Johann-type XES spectrometer was used, equipped with four spherically bent Ge (8 8 0) analyzer crystals aligned on intersecting Rowland circles. The XES spectrometer was internally calibrated using the emission lines of gray elemental selenium ($K\beta_1$ = 12488.6 eV; $K\beta_3$ = 12494.0 eV; $K\beta_2$ = 12651.1 eV). $K\beta_1$-detected XAS and $K\beta$ XES data collection was done using a dead-time corrected silicon drift diode detector (Ketek) aligned on the Rowland circle. Attenuation of the fluorescence signal was reduced by placing a He-filled flight path between the sample, the analyzer crystals, and the detector. Measurements were performed in a liquid helium flow cryostat maintained at ~20 K.

Se $K\beta$ HERFD XAS was collected over an energy range of 12640 - 12700 eV in 0.1 eV steps. The incident energy was set to 13000 eV to collect non-resonant Se $K\beta$ XES. Emission scans were collected varying the scan parameters in 3 different rages: 12485-12510 eV, 12505-12640 eV, and 12640-12670, using energy step sizes of 0.5 eV, 1.0 eV, and 0.5 eV, respectively. The total energy resolution was estimated to be approximately 1.5 eV based on the full-width at half-maximum of the elastic peaks. The width of the elastic peak (ΔE) results from a convolution of the spectrometer and monochromator resolution.

Radiation damage studies were performed on each individual sample by collecting successive fast energy range XAS scans (10 sec/scan) at a single spot on the sample, using multiple spots. Maximum dwell time per spot to collect undamaged data on all samples was 30-120 seconds. The present data comprises an average of ~10 XAS scans and ~6 XES scans on each compound. Total collection time for XES measurements was ~60 minutes per sample. The long XES measurement time (relative to the short dwell times) is due to slow motor-stepping across the large spectrometer energy window (ca. 150 eV).

Individual scans showing no evidence of radiation damage were first averaged with the PyMCA software package.[29] XAS spectra were background corrected and normalized by setting the edge-jump to 1. Experimental spectra were fit in an energy range from 12,640-12,670 eV as a sum of 1-3 pseudo-Voigt functions in the pre-edge region and 3-5 pure Gaussian

functions in the edge region using an iterative least-squares Matlab script. In all cases, the fits converged to pre-edge pseudo-Voigt functions with ≤30% Lorentzian composition. All energies and areas reported are from the corresponding fits, with pre-edge areas taken as the sum of the areas of the pre-edge functions multiplied by 100. Edge energies are reported as the white line maxima and pre-edge energies are reported as intensity weighted average of the pre-edge fitting functions.

XES spectra were normalized to the integrated intensity of the $K\beta_{1,3}$ mainlines (12485-125100 eV). The intensities and energy positions of $K\beta_2$ XES data were extracted by modelling the experimental line shapes with Pseudo-Voigt functions using an iterative least-squares Matlab script. All energies (intensity weighted averages) and areas are reported from the corresponding fits, with areas taken as the sum of the areas of the fitting functions multiplied by 100.

2.3 Computational details. All geometry optimizations, ground-state and TDDFT[30-32] calculations were executed using ORCA[33-34] version 4.1. Computations were performed using the hybrid TPSSh[35-36] functional with the D3BJ[37-38] dispersion correction and CPCM[39-41] solvation model. The ZORA[42-43] relativistic approximation was used and employed the relativistically contracted def2 Ahlrichs[44-45] basis set. A triple-ζ ZORA-def2-TZVP basis set was used for all Se, Fe, and N atoms, while a double-ζ def2-SVP basis set was used for all other atoms. The RIJCOSX[46-47] approximation was used to speed up Coulomb and exchange integrals. For the complexes discussed in this work, appropriate antiferromagnetic ground states were achieved starting from a "high spin" ferromagnetic solution and employing the spinflip keyword to access the broken symmetry solution.

Computational core-level spectroscopy for XES was carried out by a ground-state DFT procedure, where transition energies are based on energy differences between one-electron Kohn-Sham orbitals, as previously reported.[48] The hybrid TDDFT calculations were performed using 100-400 roots (depending on the system) to ensure the maximum of the rising edge was calculated. Se XAS and XES spectra were plotted with applied broadenings of 2.0 eV and 5.0 eV (fwhm) and shifted by constant values of -81.3 eV and -81.0 eV, respectively. Calculated Se XAS spectra were normalized by dividing by 5.3 to reproduce the pre-edge intensities observed experimentally for the $[Fe_2Se_2]^{n+}$ complexes (n=1, 2), and calculated Se XES spectra were normalized by dividing by 120000 to reproduce the intensities observed experimentally for the

organo-selenide series. Sample input files for calculations can be found in the supporting information.

3 Results and Discussion

3.1 Se Kβ XES. Se Kβ XES corresponds to the decay processes of Se 3p $\rightarrow$ 1s and 4p $\rightarrow$ 1s emission events (Figure 1). The 3p $\rightarrow$ 1s emission event is dominated by 3p spin-orbit coupling (SOC), splitting into the Kβ$_1$ (3p$_{3/2}$ $\rightarrow$ 1s) and Kβ$_3$ (3p$_{1/2}$ $\rightarrow$ 1s) transitions. The 4p $\rightarrow$ 1s emission Kβ$_2$ is ca. 150 eV higher in energy and represents the valence-to-core transitions. As such, the Kβ$_2$ is dominated by the bonding interactions of the Se photoabsorber.

3.2 Se Kβ$_{1,3}$ mainline. The Kβ$_{1,3}$ region of the Kβ XES spectrum is split by the 3p core-hole SOC to give a spectral shape similar to S Kα XES,[49] albeit with much larger splitting of the Kβ$_{1,3}$ lines (~5.1 eV for Se Kβ$_{1,3}$ compared to ~1.2 eV for S Kα$_{1,2}$), consistent with the larger SOC of Se relative to S. The analogy of second-row transition metal Kβ XES to first-row transition metal Kα XES has previously been demonstrated.[50] Analogous to S Kα XES, the Se Kβ mainline region is anticipated to be sensitive to the relative oxidation state of selenium, though comparatively less sensitive than S Kα XES due to greater shielding of the nucleus by the Se 3d-orbitals. Figure 2 shows a comparison of the Se Kβ mainline spectra of several reduced forms of Se: [Fe$_2$Se$_2$]$^{n+}$ complexes (n=1, 2) and hydroselenide (all formally Se^{II-}) as well as elemental selenium (Se^o). Within the resolution of the experiment, all four spectra are identical, consistent with DFT calculations (1-electron method, Figure S1) that predict at most a shift of 100 meV in the 3p to 1s transition energies. Even DFT calculations for the more oxidized compounds SeO$_3^{2-}$ and SeO$_4^{2-}$ (Se^{IV} and Se^{VI}, respectively) suggest only modest shifts in the 3p to 1s transition energy, with a maximum difference of approximately 0.3 eV (from Se^o to SeO$_4^{2-}$, Figure S2). Overall, these results reveal the Se Kβ$_{1,3}$ mainline to be much less sensitive to formal oxidation state than S Kα XES (ΔE=1.43 eV[49] from Na$_2$SO$_4$ to ZnS).

3.3 Se Kβ2 valence-to-core. The Se Kβ$_2$ XES spectra of Li$_2$Se, [Et$_4$N][SeH], KSeCN, and gray elemental selenium (Se^o) are presented in Figure 3. It is immediately clear that there are dramatic and distinct changes across the series of compounds. Starting with the ionic Li$_2$Se (Figure 3, blue), the Kβ$_2$ spectra reveals an intense symmetric feature centered at 12651 eV. Addition of a single covalent bond to selenium results in a distinctly asymmetric Kβ$_2$ spectrum, as evidenced by [Et$_4$N][SeH] (red) and KSeCN (green), with the more intense feature shifted to higher energy (ca. 12652 and 12653 eV, respectively) and a significant

shoulder shifted to lower energy (ca. 12649 eV). Finally, the fully covalent Se^o Kβ$_2$ spectrum reveals a broadened, slightly asymmetric emission feature of lower intensity centered around 12651 eV. These spectra can easily be understood from a simplistic molecular orbital (MO) diagram picture, as detailed below.

Starting at the atomic limit of selenide (Se^{2-}), the three 4p donor orbitals (4p$_x$, 4p$_y$, and 4p$_z$) are degenerate, resulting in a single, narrow valence-to-core transition in Li$_2$Se. Upon protonation to form hydroselenide (SeH^{1-}), the more positive charge on Se (2- to 1-) will result in a stabilization of the 1s orbital (due to increased Z$_{eff}$), resulting in a shift of the 4p-to-1s transition to higher energy. Additionally, mixing of a Se 4p orbital with the H 1s orbital results in a bonding MO that is filled and stabilized relative to the Se 4p energy level, as well as an unfilled antibonding MO that is destabilized relative to the Se 4p energy level. Thus, the Se valence-to-core XES spectrum will have two main transitions, one shifted to lower energy (relative to the Se^{2-} spectrum) arising from the Se–H bonding interaction, and the second transition shifted to higher energy (relative to the Se^{2-} spectrum) arising from the two remaining non-bonding Se 4p orbitals. The relative intensity of the non-bonding transition will be approximately 2/3 the intensity of the Se^{2-} spectrum, while the Se–H transition will be less than half of the non-bonding transition (as the overlap of the bonding MO with the Se 1s orbital has decreased relative to the non-bonding Se 4p atomic-like orbital). A similar MO picture can be drawn for SeCN^{1-}, resulting in qualitatively similar transitions arising from the non-bonding Se 4p orbitals and the Se–C$_\sigma$ bonding orbital, with the expectation that the more electronegative CN group will further stabilize the Se 1s orbital resulting in a shift of the Se 4p-to-1s transition to even higher energy, and the stronger Se–C bond will result in a shift to lower energy of the Se–C$_\sigma$ bonding transition. Additionally, the Se p-orbitals can mix with both the CN$_\pi$ and CN$_{\pi^*}$ orbitals, giving rise to two bonding transitions in the Se VtC XES. These simple pen-and-paper calculations are borne out by our DFT calculations, which well-match the experimental results (Figure 3).

For elemental selenium, the simple MO picture becomes slightly more complicated due its oligomeric nature. However, we can assume a set of filled Se–Se bonding orbitals (and corresponding empty antibonding orbitals), as well as a set of largely non-bonding orbitals, giving rise to two broad regions in the Se VtC XES spectrum, matching well the experimentally observed asymmetric Se^o VtC XES spectrum (Figure 3, black). DFT calculations of a model system (a linear

HSe(Se)$_6$SeH molecule was employed and the VtC spectrum was calculated for the two single central Se atoms) well-reproduce the experimental spectrum, evidencing the more complicated MO picture due to a large amount of covalent mixing with neighboring Se centers in the oligomeric structure (compare calculated individual transitions shown as black vertical sticks in Figure 3).

Quantitatively, we can also observe that overall intensity (total area, determined from fitting the experimental spectra, see experimental section) of the Se Kβ_2 XES spectra decreases in the order Se^{2-} > HSe^{1-} > NCSe^{1-} > Se^o, corresponding to increasing covalent bonding interactions (Table 1, Figures S3-5). This inverse correlation of Se VtC XES intensity to bonding covalency is consistent with the mechanism of VtC XES intensity, which is proportional to the transition dipole integral (the "allowedness" of the transition), the donor-acceptor orbital overlap (Se 4p/1s), and the number of electrons in the donor orbitals. As the 4p→1s transition is formally dipole allowed, the bulk of the intensity from these closed-shell main-group Se compounds arises from the 4p/1s orbital overlap. At the ionic limit of Li$_2$Se, the Se 4p orbitals are strongly localized to the Se center, maximizing Se 4p-Se 1s orbital overlap. As covalent bonds are formed between the photoabsorbing selenium and other atoms (H, C, Se), the generated bonding MOs of Se 4p-parentage are less localized to the Se, resulting in decreased Se 4p/1s overlap and thus decreasing Se Kβ_2 XES spectral intensities. In the case of Se^o, the formal loss of electrons relative to the selenide compounds results in further contraction of the Se orbitals, additionally contributing to the decrease in VtC intensity.

Turning now to FeSe clusters, we examine the effects of Fe oxidation state on the Se XES spectra of a μ-Se bridge in β-diketiminate supported [Fe$_2$Se$_2$]$^{n+}$ complexes (n=1, 2). From our simple MO picture developed through analysis of the Se VtC XES spectra above, we can qualitatively predict that the Se Kβ_2 spectra of the FeSe dimer complexes should lie somewhere between the Li$_2$Se and Se^o spectra, both in terms of lineshape and overall intensity, as the Fe–Se bonding interactions are assumed to be more covalent than the highly ionic Li$_2$Se, but less covalent than elemental selenium. Indeed, as experimentally observed in Figure 4, the spectra of the FeSe dimers are intermediate in intensity between Li$_2$Se and Se^o, while lacking the large asymmetry present in [Et$_4$N][SeH] and KSeCN, consistent with two Fe–Se bonding interactions. Interestingly, there is little obvious change in the Se VtC spectrum upon one-electron redox of the dimer. DFT calculations reproduce this observation,

with the mixed-valent dimer [Fe$_2$Se$_2$]$^+$ having only slightly increased intensity relative to the diferric complex [Fe$_2$Se$_2$]$^{2+}$. Experimentally, the [Fe$_2$Se$_2$]$^+$ complex also exhibits a slightly more intense Se VtC spectrum than the [Fe$_2$Se$_2$]$^{2+}$ complex (area=930 for [Fe$_2$Se$_2$]$^+$ vs 890 for [Fe$_2$Se$_2$]$^{2+}$). This slight increase in intensity for [Fe$_2$Se$_2$]$^+$ relative to [Fe$_2$Se$_2$]$^{2+}$ is again consistent with the decreased covalency of the Fe–Se bonds in the reduced dimer.

3.4 Kβ HERFD XAS. In order to maximize the information content available through measuring Se Kβ XES, we also explored Se Kβ high energy resolution fluorescence detection XAS (or Kβ HERFD XAS) using the same experimental setup. Analogous to Se Kα HERFD XAS[21-22, 51] (which uses the Kα$_1$ emission), Se Kβ HERFD XAS selectively measures the Kβ$_1$ emission maximum across the Se absorption edge. In the case of Kα HERFD XAS, experimental resolution is improved approximately two-fold compared to partial fluorescence yield measurements due to the significantly longer-lived 2p core-hole lifetime relative to the 1s core-hole lifetime. Moving to Kβ HERFD XAS, the even longer-lived 3p core-hole lifetime[52] similarly could further improve spectral resolution relative to the standard PFY measurement; however, additional multi-electron decay pathways (*i.e.* Coster-Krönig transitions) could limit any improvement in resolution relative to Kα HERFD XAS. Experimentally, we find that Kα and Kβ HERFD XAS exhibit nearly identical spectral resolution, as demonstrated in Figure S8. Thus, the intrinsic increased resolution due to the longer 3p core-hole lifetime is only moderately diminished via additional decay pathways, resulting in an overall similar spectral resolution to the Kα HERFD measurement. However, Kβ emission is approximately an order of magnitude lower in intensity than Kα emission, and thus Kβ HERFD XAS will likely require longer collection times to achieve the same signal-to-noise ratio as Kα HERFD XAS, particularly with low-concentration samples.

The Kβ HERFD XAS spectra of the diferric [Fe$_2$Se$_2$]$^{2+}$ and mixed-valent [Fe$_2$Se$_2$]$^+$ complexes are presented in Figure 5. As anticipated, the diferric complex [Fe$_2$Se$_2$]$^{2+}$, reveals an intense pre-edge feature (area = 385) around 12653 eV, consistent with the more covalent Fe–Se interactions and high d-hole count (10) in the oxidized dimer core (Table 2). Upon one-electron reduction to the mixed-valent [Fe$_2$Se$_2$]$^+$ complex, the pre-edge feature decreases in intensity (area = 260) and the rising edge shifts to lower energy, with the white line maximum decreasing from 12651.56 eV in [Fe$_2$Se$_2$]$^{2+}$ to 12660.99 eV in [Fe$_2$Se$_2$]$^+$, a net change of -0.57 eV. The decrease in pre-edge intensity and shift

to lower energy of the rising edge are both consistent with a less covalent Fe–Se interaction in the reduced dimer (as well as decrease in d-hole count to 9) and overall destabilization of the 1s Se orbital due to a lower Z_{eff}. We note that the pre-edge intensity of the diferric complex $[Fe_2Se_2]^{2+}$ (area = 385) is consistent with the previously-measured Kα HERFD XAS spectra of the diferric $[^nEt_4N]_2[Fe_2Se_2(SPh)_4]$ (370) as well as the Se_{2B} spectrum of resting-state FeMoco in nitrogenase (385 ± 20), which has been assigned as an antiferromagnetically coupled diferric site.[21] The present results further support this assignment.

The dramatic change in pre-edge intensity in the Kβ HERFD XAS spectrum upon one-electron redox of the $[Fe_2Se_2]^{n+}$ core, in contrast to the negligible intensity difference observed in the Kβ XES spectra, requires additional investigation and discussion. We turn now to DFT calculations to better elucidate the disparity.

3.5 Theoretical investigations of $[Fe_2SSe]^{n+}$ and $[Fe_2S(SeH)]^{n+}$ systems. To better understand the dramatic differences in the effects of oxidation state changes between Se XES (where there is minimal effect) and XAS (where there is significant effect) in our measured $[Fe_2Se_2]^{n+}$ dimers, we have computationally investigated a similar set of fictitious $[Fe_2SSe(SMe)_4]^{n-}$ (n=2,3) complexes. This fictitious dimer system exhibits nearly identical Se XES and XAS spectra to the experimentally investigated compounds (Figure S9), demonstrating the minimal perturbative effect of substituting the bridging (S vs Se) and terminal (thiolate vs nacnac) ligands, and the accompanying geometric changes, on the properties of the Se XES and XAS spectra. Analysis of the Se 4p orbitals via the intrinsic atom orbitals and intrinsic bonding orbitals (IAOIBO) method[53] reveals the Fe–Se bonding orbitals are on average 75.1% Se composition (Löwdin) in the oxidized dimer and 76.4% Se composition in the mixed-valent dimer, while the remaining non-bonding orbitals are 85.6% and 86.6% Se, respectively (Figures S10-11). These MO analyses are consistent with the experimental Se VtC XES spectra of the $[Fe_2Se_2]^{n+}$ complexes (n=1, 2), wherein minimal change in Se composition of the Fe–Se bonding and Se non-bonding MOs upon one electron redox results in a correspondingly minimal change in the VtC spectra.

Contrastingly, analysis of the Fe 3d manifold reveals a similarly small change (in absolute terms) of the Se contributions to the MOs upon one-electron redox, from an average of 6.44% Se p character in the oxidized dimer to 5.28% (Δ = -1.16%) in the mixed-valent dimer, well-mirroring the change in Se orbital contribution to the Fe–Se bonding MOs upon one-electron

redox from 75.1% to 76.4% (Δ = +1.3%). In the case of the Fe–Se bonding MOs, the change in Se orbital contribution has a negligible effect on the Se VtC spectra as the Se contribution (and by extension the Se 4p/1s orbital overlap) only changes in relative terms by approximately 2%; however, the same absolute magnitude change (ca. 1%) in Se orbital contribution to the Fe 3d manifold results in a more dramatic change in the XAS pre-edge intensity, as the *relative* change in Se orbital contribution is more substantial in the Fe 3d manifold MOs (ca. 20%). This implies that the significant intensity of the XAS pre-edge feature in the diferric complex is dominated by the large number of acceptor orbitals (10 half-filled Fe 3d orbitals) rather than a large Fe/Se orbital overlap, and thus the large decrease in XAS pre-edge intensity upon one-electron reduction to the mixed-valent dimer is driven less by the decrease in the number of acceptor orbitals (9 down from 10, a factor of 0.9) and more by the large relative decrease in Se p orbital contribution (5.28% down from 6.44%, a factor of 0.82) and by extension the Se 4p/1s overlap. Indeed, the product of these two ratios (0.9 x 0.82 = 0.739) well-approximates the decrease in pre-edge intensity experimentally observed upon one-electron reduction (260 ÷ 385 = 0.675). Overall, it is the relatively ionic nature of these orbitals that minimizes the effects of oxidation state changes in the Se VtC XES spectra, in contrast to the large changes observed in the corresponding Se XAS spectra.

While Se VtC XES shows little sensitivity to Fe oxidation state in FeSe complexes, we have shown experimentally that it *is* sensitive to selenium protonation (see section 3.3). Here, we further investigate computationally the utility of Se VtC XES and XAS as probes of selenium protonation in FeSe complexes using our fictitious $[Fe_2SSe]^{n+}$ complexes to yield the corresponding $[Fe_2S(SeH)]^{(n+1)+}$ complexes. In the VtC XES spectra (Figure 6), protonation of the bridging selenide yields new emission features arising from the Se–H$_\sigma$ donor orbital, which appear at lower energy (ca. 12649 eV) concomitant with loss of intensity at higher energy (ca. 12651 eV). These changes are consistent with loss of the formal Se lone-pair transition upon protonation. Similar to the unprotonated system, the calculated Se VtC XES spectra reveal no sensitivity to one-electron redox, indicating VtC XES to be a more selective probe of selenium protonation (*vide infra*). In the XAS spectrum, protonation of the selenide bridge results in a decrease in the pre-edge feature and the appearance of a new absorption feature in the rising edge assigned to the Se 1s → Se–H$_{\sigma*}$ transition. Similar trends in Fe oxidation state occur with the

$[Fe_2S(SeH)]^{(n+1)+}$ series, with decreasing pre-edge intensity with decreasing Fe oxidation state, as well as shifts in the rising edge to lower energy with decreasing oxidation state. Additionally, the $Se–H_{\sigma*}$ transition also shifts to lower energy with decreasing Fe oxidation state, consistent with destabilization of the Se 1s orbital due to a higher Z_{eff}. These results reveal that both valence-to-core XES and XAS are sensitive to Se protonation in FeSe dimers, while only XAS is sensitive to changes in redox levels. As protonation often accompanies one-electron reduction in biological cofactors,[54-55] Se XES would more cleanly evidence a protonation event regardless of any redox change, while Se XAS would reveal the convolution of the protonation event *and* the redox change, potentially resulting in the protonation event being obscured. For this hypothetical, the XAS experiment may be difficult to interpret in isolation, but combined with XES the two effects could be more easily deconvoluted.

4 Conclusions

Through investigating a series of reduced Se compounds, we have demonstrated the sensitivity of Se $K\beta_2$ VtC XES to changes in the covalent bonding interactions of the photoabsorbing Se center. The observed experimental changes can easily be rationalized through simple MO analyses and are well-reproduced through DFT calculations. The Se $K\beta_{1,3}$ mainline region reveals negligible changes in the reduced forms of Se investigated in this study (Se^{2-} and Se^o), which are also well-matched by simple DFT calculations. Se $K\beta_2$ VtC XES spectra of $[Fe_2Se_2]^{n+}$ dimers revealed minor sensitivity to changes in Fe oxidation state, in contrast to the high sensitivity of Se $K\beta$ HERFD XAS. Computational analyses reveal the source of these contrasting sensitivities arises from the relatively ionic nature of the Fe–Se bonding interactions. Additionally, the sensitivity of Se VtC XES to protonation suggests a combined Se $K\beta$ XES/$K\beta$ HERFD XAS approach could be a powerful tool in elucidating protonation/alkylation of Se within FeSe clusters, most notably in Se-substituted nitrogenase.[56-57] Furthermore, we have demonstrated that Se $K\beta$ HERFD XAS exhibits spectral resolution matching Se $K\alpha$ HERFD XAS, and thus a single experimental setup allows access to complementary Se VtC XES and HERFD XAS measurements. Future studies will explore resonant measurements as a means of enhancing sensitivity to changes in chemical and electronic structure- analogous to recent Fe resonant X-ray emission spectroscopic studies-[58] as well as the feasibility of laboratory-based Se X-ray emission measurements.

REFERENCES

1.   Lu, J.; Holmgren, A., Selenoproteins*. *Journal of Biological Chemistry* **2009,** *284* (2), 723-727.

2.   Reeves, M. A.; Hoffmann, P. R., The human selenoproteome: recent insights into functions and regulation. *Cellular and Molecular Life Sciences* **2009,** *66* (15), 2457-2478.

3.   Solovyev, N. D., Importance of selenium and selenoprotein for brain function: From antioxidant protection to neuronal signalling. *Journal of Inorganic Biochemistry* **2015,** *153,* 1-12.

4.   Nancharaiah, Y. V.; Lens, P. N. L., Ecology and Biotechnology of Selenium-Respiring Bacteria. *Microbiology and Molecular Biology Reviews* **2015,** *79* (1), 61.

5.   Chaudhary, S.; Mehta, S. K., Selenium Nanomaterials: Applications in Electronics, Catalysis and Sensors. *Journal of Nanoscience and Nanotechnology* **2014,** *14* (2), 1658-1674.

6.   Korde, P.; Ghotekar, S.; Pagar, T.; Pansambal, S.; Oza, R.; Mane, D., Plant Extract Assisted Eco-benevolent Synthesis of Selenium Nanoparticles- A Review on Plant Parts Involved, Characterization and Their Recent Applications. *Journal of Chemical Reviews* **2020,** *2* (3), 157-168.

7.   Dou, L.; Chang, W.-H.; Gao, J.; Chen, C.-C.; You, J.; Yang, Y., A Selenium-Substituted Low-Bandgap Polymer with Versatile Photovoltaic Applications. *Advanced Materials* **2013,** *25* (6), 825-831.

8.   Hadar, I.; Song, T.-B.; Ke, W.; Kanatzidis, M. G., Modern Processing and Insights on Selenium Solar Cells: The World's First Photovoltaic Device. *Advanced Energy Materials* **2019,** *9* (16), 1802766.

9.   Kunioka, A.; Nakada, T., High-Efficiency Selenium Photovoltaic Solar Cells. *Japanese Journal of Applied Physics* **1982,** *21* (S2), 73.

10.   Eftekhari, A., The rise of lithium–selenium batteries. *Sustainable Energy & Fuels* **2017,** *1* (1), 14-29.

11.   Zhou, J.; Yang, J.; Xu, Z.; Zhang, T.; Chen, Z.; Wang, J., A high performance lithium–selenium battery using a microporous carbon confined selenium cathode and a compatible electrolyte. *Journal of Materials Chemistry A* **2017,** *5* (19), 9350-9357.

12.   Block, E.; Glass, R. S.; Jacobsen, N. E.; Johnson, S.; Kahakachchi, C.; Kamiński, R.; Skowrońska, A.; Boakye, H. T.;

Tyson, J. F.; Uden, P. C., Identification and Synthesis of a Novel Selenium–Sulfur Amino Acid Found in Selenized Yeast: Rapid Indirect Detection NMR Methods for Characterizing Low-Level Organoselenium Compounds in Complex Matrices. *Journal of Agricultural and Food Chemistry* **2004,** *52* (12), 3761-3771.

13. Mobli, M.; Morgenstern, D.; King, G. F.; Alewood, P. F.; Muttenthaler, M., Site-Specific pKa Determination of Selenocysteine Residues in Selenovasopressin by Using 77Se NMR Spectroscopy. *Angewandte Chemie International Edition* **2011,** *50* (50), 11952-11955.

14. Ogra, Y., Integrated strategies for identification of selenometabolites in animal and plant samples. *Analytical and Bioanalytical Chemistry* **2008,** *390* (7), 1685-1689.

15. Ogra, Y.; Kitaguchi, T.; Ishiwata, K.; Suzuki, N.; Toida, T.; Suzuki, K. T., Speciation of selenomethioninemetabolites in wheat germ extract. *Metallomics* **2009,** *1* (1), 78-86.

16. Ramadan, S. E.; Razak, A. A.; Yousseff, Y. A.; Sedky, N. M., Selenium metabolism in a strain of Fusarium. *Biological Trace Element Research* **1988,** *18* (1), 161.

17. Schaefer, S. A.; Dong, M.; Rubenstein, R. P.; Wilkie, W. A.; Bahnson, B. J.; Thorpe, C.; Rozovsky, S., 77Se Enrichment of Proteins Expands the Biological NMR Toolbox. *Journal of Molecular Biology* **2013,** *425* (2), 222-231.

18. Suzuki, K. T.; Doi, C.; Suzuki, N., Simultaneous tracing of multiple precursors each labeled with a different homo-elemental isotope by speciation analysis: Distribution and metabolism of four parenteral selenium sources. *Pure and Applied Chemistry* **2008,** *80* (12), 2699-2713.

19. Suzuki, N.; Ogra, Y., 77Se NMR Spectroscopy for Speciation Analysis of Selenium Compounds. In *Metallomics: Recent Analytical Techniques and Applications*, Ogra, Y.; Hirata, T., Eds. Springer Japan: Tokyo, 2017; pp 147-155.

20. Pickering, I. J.; Brown, G. E.; Tokunaga, T. K., Quantitative Speciation of Selenium in Soils Using X-ray Absorption Spectroscopy. *Environmental Science & Technology* **1995,** *29* (9), 2456-2459.

21. Henthorn, J. T.; Arias, R. J.; Koroidov, S.; Kroll, T.; Sokaras, D.; Bergmann, U.; Rees, D. C.; DeBeer, S., Localized Electronic Structure of Nitrogenase FeMoco Revealed by Selenium K-Edge High Resolution X-ray Absorption Spectroscopy. *Journal of the American Chemical Society* **2019,** *141* (34), 13676-13688.

22. Nehzati, S.; Dolgova, N. V.; James, A. K.; Cotelesage, J. J. H.; Sokaras, D.; Kroll, T.; George, G. N.; Pickering, I. J., High Energy Resolution Fluorescence Detected X-ray Absorption Spectroscopy: An Analytical Method for Selenium Speciation. *Analytical Chemistry* **2021,** *93* (26), 9235-9243.

23. de Souza, M. P.; Amini, A.; Dojka, M. A.; Pickering, I. J.; Dawson, S. C.; Pace, N. R.; Terry, N., Identification and Characterization of Bacteria in a Selenium-Contaminated Hypersaline Evaporation Pond. *Applied and Environmental Microbiology* **2001,** *67* (9), 3785-3794.

24. Ellis, D. R.; Sors, T. G.; Brunk, D. G.; Albrecht, C.; Orser, C.; Lahner, B.; Wood, K. V.; Harris, H. H.; Pickering, I. J.; Salt, D. E., Production of Se-methylselenocysteine in transgenic plants expressing selenocysteine methyltransferase. *BMC Plant Biology* **2004,** *4* (1), 1.

25. Tokunaga, T. K.; Pickering, I. J.; Brown Jr, G. E., Selenium Transformations in Ponded Sediments. *Soil Science Society of America Journal* **1996,** *60* (3), 781-790.

26. Holden, W. M.; Jahrman, E. P.; Govind, N.; Seidler, G. T., Probing Sulfur Chemical and Electronic Structure with Experimental Observation and Quantitative Theoretical Prediction of Kα and Valence-to-Core Kβ X-ray Emission Spectroscopy. *The Journal of Physical Chemistry A* **2020,** *124* (26), 5415-5434.

27. Qureshi, M.; Nowak, S. H.; Vogt, L. I.; Cotelesage, J. J. H.; Dolgova, N. V.; Sharifi, S.; Kroll, T.; Nordlund, D.; Alonso-Mori, R.; Weng, T.-C.; Pickering, I. J.; George, G. N.; Sokaras, D., Sulfur Kβ X-ray emission spectroscopy: comparison with sulfur K-edge X-ray absorption spectroscopy for speciation of organosulfur compounds. *Physical Chemistry Chemical Physics* **2021**.

28. Henthorn, J.T.; Cutsail, G.E.; Weyhermüller, T.; DeBeer, S. Stabilization of Intermediate Spin States in Mixed-valent Diiron Dichalcogenide Complexes, in press, Nat. Chem.

29. Solé, V. A.; Papillon, E.; Cotte, M.; Walter, P.; Susini, J., A multiplatform code for the analysis of energy-dispersive X-ray fluorescence spectra. *Spectrochimica Acta Part B: Atomic Spectroscopy* **2007,** *62* (1), 63-68.

30. DeBeer George, S.; Neese, F., Calibration of Scalar Relativistic Density Functional Theory for the Calculation of Sulfur K-Edge X-ray Absorption Spectra. *Inorganic Chemistry* **2010,** *49* (4), 1849-1853.

31. DeBeer George, S.; Petrenko, T.; Neese, F., Time-dependent density functional calculations of ligand K-edge X-ray absorption spectra. *Inorganica Chimica Acta* **2008,** *361* (4), 965-972.

32. Neese, F., Prediction of molecular properties and molecular spectroscopy with density functional theory: From fundamental theory to exchange-coupling. *Coordination Chemistry Reviews* **2009,** *253* (5), 526-563.

33. Neese, F., The ORCA program system. *Wiley Interdisciplinary Reviews: Computational Molecular Science* **2012,** *2* (1), 73-78.

34. Neese, F., Software update: the ORCA program system, version 4.0. *WIREs Computational Molecular Science* **2018,** *8* (1), e1327.

35. Staroverov, V. N.; Scuseria, G. E.; Tao, J.; Perdew, J. P., Comparative assessment of a new nonempirical density functional: Molecules and hydrogen-bonded complexes. *The Journal of Chemical Physics* **2003,** *119* (23), 12129-12137.

36. Tao, J.; Perdew, J. P.; Staroverov, V. N.; Scuseria, G. E., Climbing the Density Functional Ladder: Nonempirical Meta--Generalized Gradient Approximation Designed for Molecules and Solids. *Physical Review Letters* **2003,** *91* (14), 146401.

37. Grimme, S.; Antony, J.; Ehrlich, S.; Krieg, H., A consistent and accurate ab initio parametrization of density functional dispersion correction (DFT-D) for the 94 elements H-Pu. *The Journal of Chemical Physics* **2010,** *132* (15), 154104.

38. Grimme, S.; Ehrlich, S.; Goerigk, L., Effect of the damping function in dispersion corrected density functional theory. *Journal of Computational Chemistry* **2011,** *32* (7), 1456-1465.

39. Barone, V.; Cossi, M., Quantum Calculation of Molecular Energies and Energy Gradients in Solution by a Conductor Solvent Model. *The Journal of Physical Chemistry A* **1998,** *102* (11), 1995-2001.

40. Garcia-Ratés, M.; Neese, F., Efficient implementation of the analytical second derivatives of hartree–fock and hybrid DFT energies within the framework of the conductor-like polarizable continuum model. *Journal of Computational Chemistry* **2019,** *40* (20), 1816-1828.

41. Pascual-Ahuir, J. L.; Silla, E., GEPOL: An improved description of molecular surfaces. I. Building the spherical surface set. *Journal of Computational Chemistry* **1990,** *11* (9), 1047-1060.

42. Lenthe, E. v.; Baerends, E. J.; Snijders, J. G., Relativistic regular two-component Hamiltonians. *The Journal of Chemical Physics* **1993,** *99* (6), 4597-4610.

43. van Wüllen, C., Molecular density functional calculations in the regular relativistic approximation: Method, application to coinage metal diatomics, hydrides, fluorides and chlorides, and comparison with first-order relativistic calculations. *The Journal of Chemical Physics* **1998,** *109* (2), 392-399.

44. Pantazis, D. A.; Chen, X.-Y.; Landis, C. R.; Neese, F., All-Electron Scalar Relativistic Basis Sets for Third-Row Transition Metal Atoms. *Journal of Chemical Theory and Computation* **2008,** *4* (6), 908-919.

45. Weigend, F.; Ahlrichs, R., Balanced basis sets of split valence, triple zeta valence and quadruple zeta valence quality for H to Rn: Design and assessment of accuracy. *Physical Chemistry Chemical Physics* **2005,** *7* (18), 3297-3305.

46. Izsák, R.; Neese, F., An overlap fitted chain of spheres exchange method. *The Journal of Chemical Physics* **2011,** *135* (14), 144105.

47. Neese, F.; Wennmohs, F.; Hansen, A.; Becker, U., Efficient, approximate and parallel Hartree–Fock and hybrid DFT calculations. A 'chain-of-spheres' algorithm for the Hartree–Fock exchange. *Chemical Physics* **2009,** *356* (1), 98-109.

48. Lee, N.; Petrenko, T.; Bergmann, U.; Neese, F.; DeBeer, S., Probing Valence Orbital Composition with Iron Kβ X-ray Emission Spectroscopy. *Journal of the American Chemical Society* **2010,** *132* (28), 9715-9727.

49. Alonso Mori, R.; Paris, E.; Giuli, G.; Eeckhout, S. G.; Kavčič, M.; Žitnik, M.; Bučar, K.; Pettersson, L. G. M.; Glatzel, P., Electronic Structure of Sulfur Studied by X-ray Absorption and Emission Spectroscopy. *Analytical Chemistry* **2009,** *81* (15), 6516-6525.

50. Castillo, R. G.; Henthorn, J. T.; McGale, J.; Maganas, D.; DeBeer, S., Kβ X-Ray Emission Spectroscopic Study of a Second-Row Transition Metal (Mo) and Its Application to Nitrogenase-Related Model Complexes. *Angewandte Chemie International Edition* **2020,** *59* (31), 12965-12975.

51. Nehzati, S.; Dolgova, N. V.; Sokaras, D.; Kroll, T.; Cotelesage, J. J. H.; Pickering, I. J.; George, G. N., A Photochemically Generated Selenyl Free Radical Observed by High Energy Resolution Fluorescence Detected X-ray Absorption Spectroscopy. *Inorganic Chemistry* **2018,** *57* (17), 10867-10872.

52. Krause, M. O.; Oliver, J. H., Natural widths of atomic K and L levels, Kα X-ray lines and several KLL Auger lines. *Journal of Physical and Chemical Reference Data* **1979,** *8* (2), 329-338.

53. Knizia, G., Intrinsic Atomic Orbitals: An Unbiased Bridge between Quantum Theory and Chemical Concepts. *Journal of Chemical Theory and Computation* **2013,** *9* (11), 4834-4843.

54. Chang, C. J.; Chang, M. C. Y.; Damrauer, N. H.; Nocera, D. G., Proton-coupled electron transfer: a unifying mechanism for biological charge transport, amino acid radical initiation and propagation, and bond making/breaking reactions of water and oxygen. *Biochimica et Biophysica Acta (BBA) - Bioenergetics* **2004,** *1655*, 13-28.

55. Reece, S. Y.; Nocera, D. G., Proton-Coupled Electron Transfer in Biology: Results from Synergistic Studies in Natural and Model Systems. *Annual Review of Biochemistry* **2009,** *78* (1), 673-699.

56. Spatzal, T.; Perez, K. A.; Howard, J. B.; Rees, D. C., Catalysis-dependent selenium incorporation and migration in the nitrogenase active site iron-molybdenum cofactor. *eLife* **2015,** *4*, e11620.

57. Morrison, C. N.; Spatzal, T.; Rees, D. C., Reversible Protonated Resting State of the Nitrogenase Active Site. *Journal of the American Chemical Society* **2017,** *139* (31), 10856-10862.

58. Castillo, R. G.; Hahn, A. W.; Van Kuiken, B. E.; Henthorn, J. T.; McGale, J.; DeBeer, S., Probing Physical Oxidation State by Resonant X-ray Emission Spectroscopy: Applications to Iron Model Complexes and Nitrogenase. *Angewandte Chemie International Edition* **2021,** *60* (18), 10112-10121.
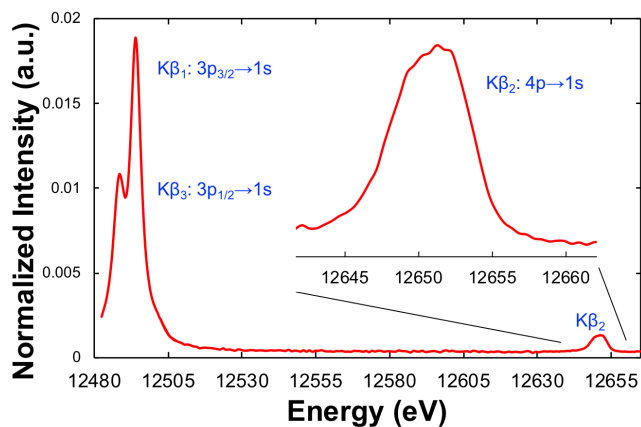
Figure 1. Full Se Kβ XES spectrum of gray elemental selenium, including the Kβ₁,₃ mainline and Kβ₂ valence-to-core regions. Inset shows Kβ₂ region in greater detail.

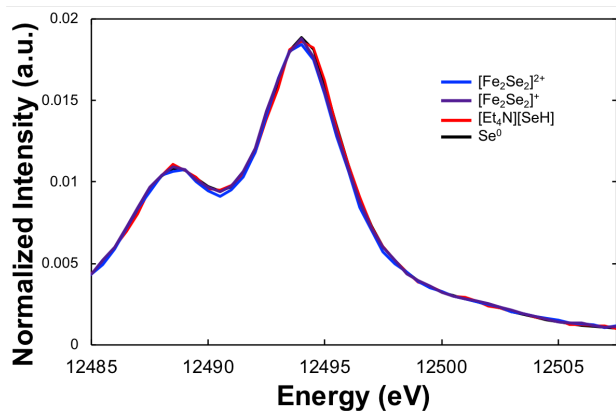**Figure 2.** Se Kβ mainline (Kβ₁,₃) comparison of four reduced selenium compounds: $[Fe_2Se_2]^{2+}$ (blue), $[Fe_2Se_2]^+$ (purple), $[Et_4N][SeH]$ (red), and elemental selenium (black).
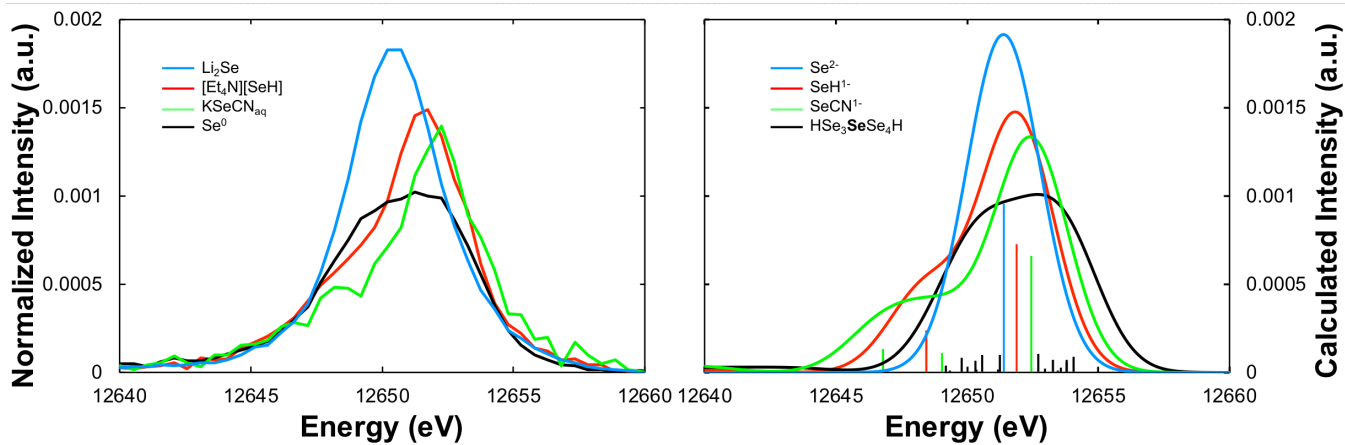

Figure 3. Background-subtracted experimental (left) and DFT calculated (right) Se valence-to-core spectra of Li_2Se (light blue), $[Et_4N][SeH]$ (red), KSeCN (green), and elemental selenium (black). Individual calculated transitions are shown as vertical sticks, while line-broadened spectra are shown as curves.

Table 1. Se K VtC XES energies and areas

Sample	energy [a] (eV)	area
Li_2Se	12650.54	960
$[Et_4N][SeH]$	12650.90	820
KSeCN	12651.25	740
Se^o	12650.42	730
$[Fe_2Se_2]^{2+}$	12650.76	890
$[Fe_2Se_2]^+$	12650.70	930

[a] Area-weighted average of fitting functions

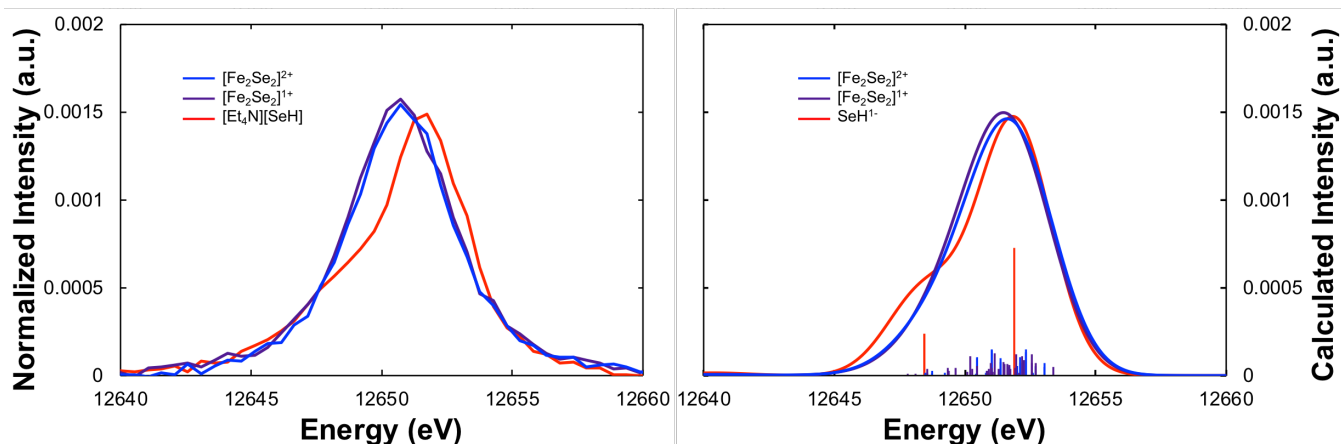**Figure 4.** Background-subtracted experimental (left) and DFT calculated (right) Se valence-to-core spectra of $[Fe_2Se_2]^{2+}$ (blue), $[Fe_2Se_2]^+$ (purple), and $[Et_4N][SeH]$ (red). Individual calculated transitions are shown as vertical sticks, while line-broadened spectra are shown as curves.
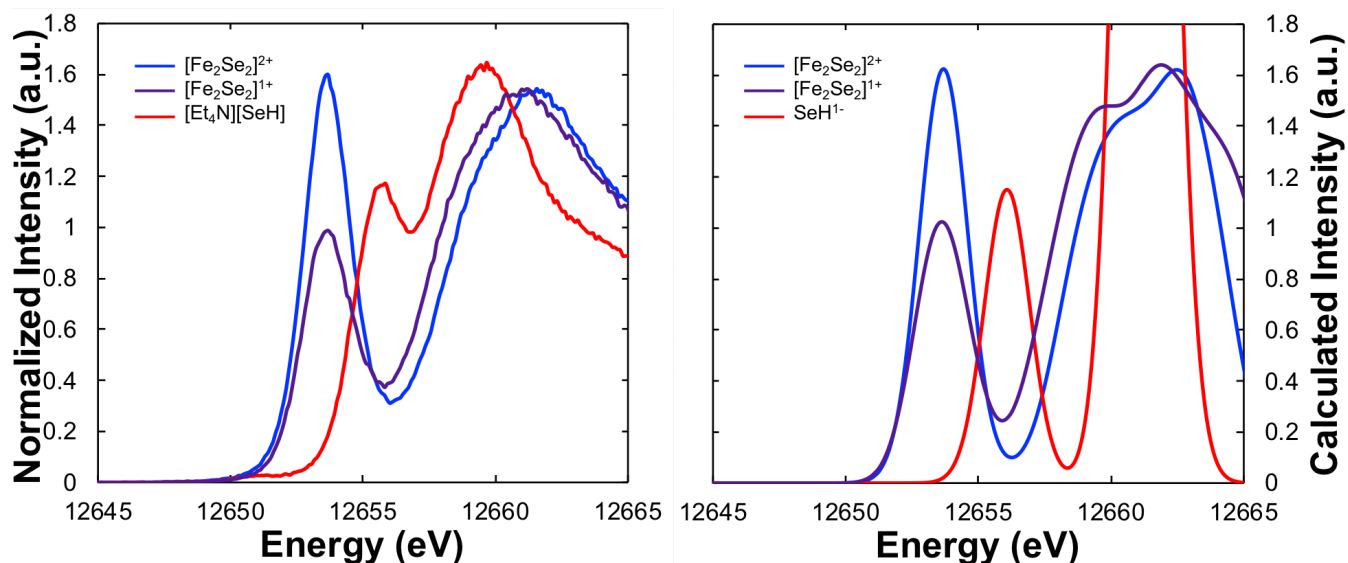

Figure 5. Experimental (left) and TDDFT calculated (right) $K\beta_1$ HERFD XAS spectra of $[Fe_2Se_2]^{2+}$ (blue), $[Fe_2Se_2]^+$ (purple), and $[SeH]^{1-}$ (red).

Table 2. Se Kβ₁ HERFD XAS edge energies, pre-edge energies and areas, and relative Fe 3d-manifold energies

	edge	pre-edge		
Sample	energy (eV)	energy (eV)	Area	$|\delta_d|^a$ (eV)
$[Fe_2Se_2]^{2+}$	12661.56	12653.70	385	7.86
$[Fe_2Se_2]^+$	12660.99	12653.73	260	7.26
$[Et_4N][SeH]$	12659.57	12655.47	260	--
Se^o	12663.72	12655.87	740	--

$^a|\delta_d| = |(\text{pre-edge energy}) - (\text{edge energy})|$
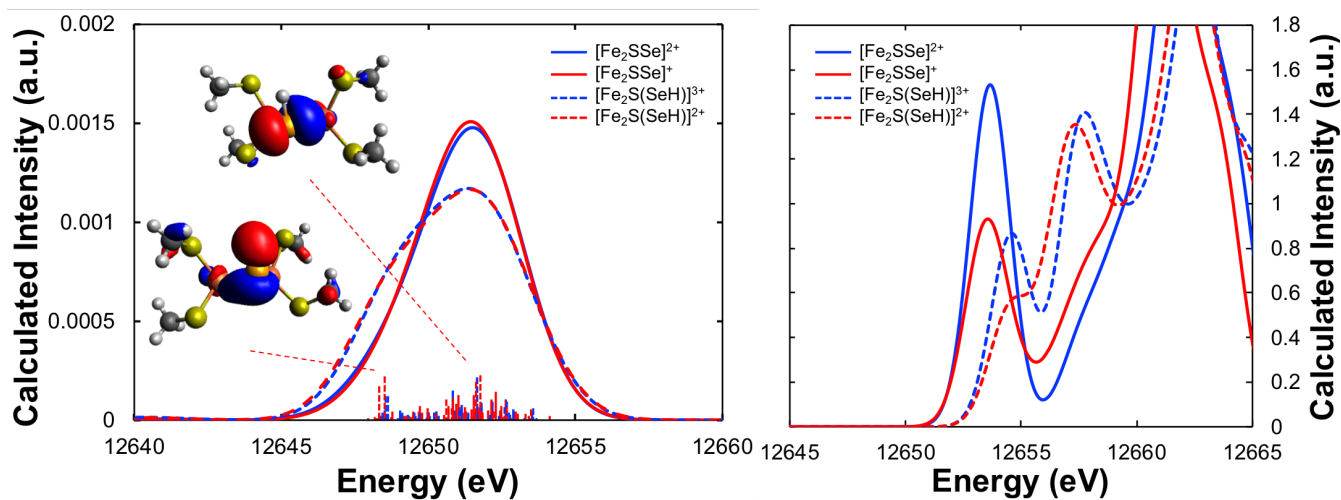

Figure 6. Calculated Se VtC XES (left) and XAS (right) spectra of fictitious $[Fe_2SSe]^{2+}$ (solid blue), $[Fe_2SSe]^+$ (solid red), $[Fe_2S(SeH)]^{3+}$ (dashed blue), and $[Fe_2S(SeH)]^{2+}$ (dashed red). Individual transitions are shown as vertical sticks. Inset shows MOs corresponding to the Fe–Se$_\sigma$ donor transition and the Se–H$_\sigma$ donor transition for the $[Fe_2S(SeH)]^{2+}$ complex.